J. Fluid Mech. (1993), *vol.* 247, *pp.* 247–274

Hydrodynamic instabilities in cylindrical thermocapillary liquid bridges

By H. C. KUHLMANN AND H. J. RATH

Center of Applied Space Technology and Microgravity, ZARM – University of Bremen, 2800 Bremen 33, Germany

(Received 2 January 1992 and in revised form 24 August 1992)

The hydrodynamic stability of steady axisymmetric thermocapillary flow in a cylindrical liquid bridge is investigated by linear stability theory. The basic state and the three-dimensional disturbance equations are solved by various spectral methods for aspect ratios close to unity. The critical modes have azimuthal wavenumber one and the most dangerous disturbance is either a pure hydrodynamic steady mode or an oscillatory hydrothermal wave, depending on the Prandtl number. The influence of heat transfer through the free surface, additional buoyancy forces, and variations of the aspect ratio on the stability boundaries and the neutral mode are discussed.

1. Introduction

A particular type of convection arises if part of the bounding surface of a volume of liquid is subject to tangential stresses. These stresses can be due to a non-uniform surface tension along the interface of two immiscible liquids, and may be caused by a spatial variation of the surface temperature or chemical composition. In the case of tangential temperature gradients the resulting flow is called thermocapillary convection.

Thermocapillary-force-driven flows have received increasing attention in crystal growth and materials science during the past decade. In particular, in the containerless method of float-zone crystal-growth, where a free surface with surface tension is utilized to support a hot cylinder-like volume of molten material between the colder ends of a feed and seed crystal, the required temperature gradients drive thermocapillary convection in the melt. This flow becomes dominant over buoyant convection if the liquid volume is small or if the process is conducted in a low-gravity environment. Sometimes, a certain degree of convection is desired to avoid macrosegregation. However, as spatio–temporal flows evolve due to an increased temperature gradient, undesired inhomogeneities in composition of the single crystal can result (for recent experiments, see Cröll *et al.* 1991). For a better understanding and optimization of these crystal growth processes, model problems have been developed and some are now studied as paradigms similar to, for example, the related driven-cavity problem.

One of the major difficulties in the theoretical modelling of crystal growth is that the geometry of the boundary of the liquid volume is not known *a priori*. Phase changes due to melting and solidification pose a Stefan problem and also the position of the free surface has to be determined as a part of the solution. In addition the non-isothermal, often multicomponent, fluid is subject to coupled thermo- and solutocapillary convection as well as, in the presence of gravity, multicomponent buoyant convection. Finally, heat loss to the environment can be conductive,

convective and radiative. When studying primarily thermocapillary convection some of these difficulties can be circumvented by considering non-isothermal liquid bridges. The most common model is that of a cylindrical liquid bridge formed by a liquid drop suspended between two rigid planar circular disks. Driving of the flow is provided by keeping the disks at different temperatures or by imposing some temperature distribution on the free surface.

The strength of thermocapillary convection is determined by the maximum absolute value of the tangential temperature gradient occurring in the system. For fluids with small Prandtl number the corresponding dimensionless parameter is the surface tension Reynolds number

$$Re = \frac{\gamma d \Delta T}{\rho \nu^2}, \tag{1.1}$$

where ρ and ν are the density and kinematic viscosity of the fluid, γ is the negative slope of the surface tension with respect to the temperature, and d and ΔT are the characteristic linear dimension and an imposed temperature variation. For high Prandtl numbers Pr even weak convection can lead to a convective crowding of isotherms and to localized steep temperature gradients. Hence, the Marangoni number $Ma = Re\,Pr$ is the appropriate parameter if Pr is large.

For creeping flow ($Re \ll 1$) Rybicki & Floryan (1987) have calculated the steady two-dimensional thermocapillary convection numerically in the limit of zero Prandtl number for cylindrical liquid bridges with different imposed temperature profiles and aspect ratios. The main conclusion drawn is that, for small driving, the flow consists of one or more Moffat eddies, the detailed structure depending on the geometry and the external heat load. Kuhlmann (1989) solved the Stokes flow problem analytically in terms of a biorthogonal series for small Prandtl number, also giving the lowest-order temperature field and surface deformations. Smith (1986*a*) calculated the small Reynolds number flow with boundary-layer theory. He studied the influence of small Ekman number rotation on the flow pattern as well as the influence of weak centrifugal buoyancy.

The only analytical solution for thermocapillary flows with $Re = O(1)$ has been given by Xu & Davis (1983), who obtained similarity solutions for two-dimensional steady core flow in the limit of a slender bridge. Steady two-dimensional numerical calculations have been carried out by Chang & Wilcox (1976) and Clark & Wilcox (1980). They investigated the influence of gravity and axial throughflow on the flow in a full zone, i.e. a liquid bridge where the surface temperature attains a local maximum thereby inducing two counter-rotating vortices. Fu & Ostrach (1985) have found the flow in a half-zone with a monotonic surface temperature distribution to be essentially a single-cell flow.

A number of articles dealing with experiments on thermocapillary convection have been published. Not all can be covered here. It has been observed in model experiments (Chun 1980) that, if the Reynolds number is increased beyond a critical value, the steady two-dimensional toroidal flow undergoes a transition to a three-dimensional state which oscillates harmonically close to the onset. Preisser, Schwabe & Scharmann (1983) have shown that the periodicity of the azimuthally travelling waves depend on the aspect ratio $\tilde{\Gamma}$ of the liquid bridge. Experiments for very small Rayleigh numbers have been performed by Kamotani, Ostrach & Vargas (1984). They suggested that the free-surface deformation of the liquid bridge is an important factor causing the oscillations. More recently, Velten, Schwabe & Scharmann (1991) have done experiments using fluids of different Prandtl numbers ($Pr > 1$). They

systematically characterized the observed supercritical spatio–temporal structures of time-dependent thermocapillary convection in the $(Re, \tilde{\Gamma})$-plane and showed that the prevailing patterns are strongly influenced by the orientation of the gravitational acceleration. It was found that the critical Reynolds number for the first appearance of oscillations is increased when the liquid bridge is heated from below as compared to the critical value for heating from above.

The experimentally observed instabilities motivated further numerical studies. Rupp, Müller & Neumann (1989) have simulated the flow within a model problem using a time-dependent three-dimensional finite difference scheme. For Prandtl numbers less than unity they found stationary flows with broken axisymmetry. On increase of the Reynolds number these flows started to oscillate back and forth around the axis, contrary to the propagating waves found for Prandtl numbers larger than one. The bifurcations of steady axisymmetric flow to time-dependent axisymmetric states have been computed by Kazarinoff & Wilkowski (1990). They simulated scenarios of transition to chaotic motion under the restriction of axisymmetry. Shen *et al.* (1990) have applied energy stability theory to the basic flow in cylindrical half-zones. Critical Reynolds numbers were obtained below which the basic state is stable to axisymmetric disturbances. Recently, Neitzel *et al.* (1991) obtained energy stability limits for non-axisymmetric disturbances for $Pr = 1$ and various aspect ratios. Their stability limits are close to the experimentally determined stability boundaries of Velten *et al.* (1991). Corresponding numerical values for the linear stability boundary for $Pr = 1$ given by Neitzel *et al.* (1992), however, lie substantially above the energy limits and also above the experimentally determined transition Marangoni numbers. The linear stability of steady thermocapillary convection in an infinitely long liquid bridge has been calculated numerically by Xu & Davis (1984). For Prandtl numbers less than a critical value the critical disturbances are hydrothermal spiral waves propagating either up- or downstream of the surface flow, whereas for larger Prandtl numbers the neutral mode is an axisymmetric travelling wave. Owing to the lack of axial boundaries the predicted critical Reynolds numbers are considerably below those observed in experiments.

Numerical calculations of steady two-dimensional thermocapillary convection in other geometries have been made by Sen & Davis (1982), Zebib, Homsy & Meiburg (1985), and Carpenter & Homsy (1989). Corresponding stability calculations are due to Smith & Davis (1983*a*, *b*), Smith (1986*b*), Smith (1988), and Carpenter & Homsy (1990).

Although a considerable amount of publications on thermocapillary convection in liquid bridges has appeared over the past ten years, a coherent picture has not yet emerged. Experiments showed that axisymmetry is lost at the onset of time-dependence. Two-dimensional stability calculations yielded consistent results indicating that the basic state can loose its stability to two-dimensional flows only for Reynolds numbers well above those for modulated vortices (Shen *et al.* 1990). It was found (Rupp *et al.* 1989), moreover, that the basic state can loose axisymmetry without becoming time-dependent. These observations lead to the conclusion that the first instability is most likely to be characterized by a loss of spatial symmetry rather than the onset of time-dependence. Since no hysteresis has been detected, the instability can be expected to be a forward bifurcation. Thus linear stability theory should correctly give the stability boundary.

Here, we calculate the steady two-dimensional basic flow in a half-zone model with a mixed Galerkin–Chebyshev–Tau method. The linear stability of the toroidal basic flow is investigated by an application of linear stability theory. The stability

equations are solved spectrally to give the critical Reynolds number, azimuthal wavenumber and oscillation frequency. In §2 the mathematical model is introduced. Section 3 deals with the solution method for the basic state equations and §4 describes the method for solving the stability equations. In §5 results are presented and discussed and they are compared with previous work in §6. The main results are summarized in §7.

2. The mathematical model

The so-called half-zone model (see e.g. Shen *et al.* 1990) has often been employed to investigate the role of thermocapillary convection in float-zone crystal growth processes. This model relates very closely to experimental models (see, for instance, Preisser *et al.* 1983) and will be briefly summarized here. The flow and temperature field in a liquid bridge are considered in the Boussinesq approximation:

$$[\partial_t + \boldsymbol{u}\cdot\boldsymbol{\nabla}]\,\boldsymbol{u} = -\frac{1}{\rho}\boldsymbol{\nabla}p + \nu\boldsymbol{\nabla}^2\boldsymbol{u} + \beta g T \boldsymbol{e}_z, \tag{2.1}$$

$$\boldsymbol{\nabla}\cdot\boldsymbol{u} = 0, \tag{2.2}$$

$$[\partial_t + \boldsymbol{u}\cdot\boldsymbol{\nabla}]\,T = \kappa\boldsymbol{\nabla}^2 T. \tag{2.3}$$

Using cylindrical polar coordinates the velocity field is given by $\boldsymbol{u}(r,\phi,z,t) = u\boldsymbol{e}_r + v\boldsymbol{e}_\phi + w\boldsymbol{e}_z$. The variables T and p, and the constants $\rho, \nu, \kappa, \beta, g$ and $\boldsymbol{e}_z$ appearing in (2.1)–(2.3) denote temperature, pressure, density, kinematic viscosity, thermal diffusivity, thermal expansion coefficient, acceleration due to gravity and axial unit vector, respectively. The liquid is bounded axially by two parallel coaxial circular disks of radius R_0 separated by the distance d, which represent no-slip and no-penetration boundary conditions. Constant but different temperatures T_u and T_l are imposed on the upper and lower disks so that the axial boundary conditions are

$$\boldsymbol{u} = 0 \quad \text{on} \quad z = \pm\tfrac{1}{2}d, \tag{2.4}$$

$$T = T_\mathrm{u} \quad \text{on} \quad z = \tfrac{1}{2}d, \tag{2.5}$$

$$T = T_\mathrm{l} \quad \text{on} \quad z = -\tfrac{1}{2}d. \tag{2.6}$$

Depending on the liquid volume and forces acting, the position $r = R(\phi,z,t)$ of the free surface of the liquid is a function of the azimuthal (ϕ), axial (z) and time (t) coordinates. R has to be determined as part of the solution which must satisfy the stress balance on the interface. If shear stresses outside the liquid are neglected, this balance is given by

$$\boldsymbol{\sigma}\cdot\boldsymbol{n} + \alpha\left(\frac{1}{R_1}+\frac{1}{R_2}\right)\boldsymbol{n} - (\boldsymbol{I}-\boldsymbol{nn})\cdot\boldsymbol{\nabla}\alpha = -p_\mathrm{a}\boldsymbol{n} \quad \text{on} \quad r = R, \tag{2.7}$$

where $\boldsymbol{\sigma}$, α, R_i, $\boldsymbol{I}$, p_a and $\boldsymbol{n}$ are the stress tensor of the liquid, surface tension, main radii of curvature, identity matrix, ambient pressure and unit outward normal vector, respectively. At first order the surface tension is a linear function of temperature

$$\alpha \approx \alpha_0(T_\mathrm{m}) - \gamma(T - T_\mathrm{m}), \tag{2.8}$$

where the mean surface tension α_0 is taken at the reference temperature $T_\mathrm{m} = \frac{1}{2}(T_\mathrm{u}+T_\mathrm{l})$. Owing to the presence of temperature gradients, fluid motion is driven by buoyancy and thermocapillarity ($\boldsymbol{\nabla}\alpha$ in (2.7)). Here we consider the limit in which α_0 is asymptotically large so that the corresponding forces dominate all other

hydrodynamic and hydrostatic forces. In this limit and assuming fixed contact lines the liquid bridge takes a cylindrical shape ($R = R_0$) and the associated pressure jump is $p_0 - p_a = \alpha_0/R_0$ with p_0 being the static pressure in the liquid zone. If, furthermore, (2.8) is utilized, the stress boundary condition (2.7) can be simplified to give

$$\left.\begin{aligned} \rho\nu\partial_r w + \gamma\partial_z T &= 0 \\ \rho\nu r\partial_r(v/r) + \gamma/r\,\partial_\phi T &= 0 \\ u &= 0 \end{aligned}\right\} \quad \text{on} \quad r = R_0, \tag{2.9–2.11}$$

where (2.11) is the kinematic boundary condition. The thermal conditions at the free cylindrical surface are modelled by the heat transfer law

$$k\partial_r T + h(T - T_a(z)) = 0 \quad \text{on} \quad r = R_0, \tag{2.12}$$

where k is the thermal conductivity of the fluid and h the heat transfer coefficient. Throughout, the ambient temperature is assumed to be $T_a(z) = T_m + \Delta T z/d$ with $\Delta T = T_u - T_l$.

We are interested in the evolution of the flow as the surface tension Reynolds number Re (1.1) is increased from zero. For creeping flow ($Re \ll 1$) and small Prandtl number (2.1)–(2.6) and (2.9)–(2.12) admit stationary axisymmetric solutions with a flow in the (r, z)-plane and streamlines symmetric with respect to the midplane $z = 0$ (Kuhlmann 1989). The latter symmetry is lost for increased Reynolds or Prandtl numbers. On further increase of Re even axisymmetry is lost through a stationary or oscillatory bifurcation. In order to identify the transition boundary it is necessary to first calculate the nonlinear axisymmetric basic state.

3. Basic state calculations

We seek solutions of (2.1)–(2.3) with boundary conditions (2.4)–(2.6) and (2.9)–(2.12) that are steady and axisymmetric, i.e. $\partial_t = \partial_\phi = 0$. For this two-dimensional flow a stream function ψ is introduced such that

$$u_0 = \partial_z \psi_0, \tag{3.1}$$

$$w_0 = -\mathrm{D}_* \psi_0, \tag{3.2}$$

where the subscript 0 denotes the basic state and $\mathrm{D}_* = \mathrm{D} + 1/r = \partial_r + 1/r$ (the Stokes stream function is given by $r\psi_0$). If we further define the normalized temperature deviation from the linear conducting ($Re = 0$) profile $T_{\mathrm{cond}}(z) = T_m + \Delta T z/d$ as

$$\theta_0 = \frac{T - T_{\mathrm{cond}}(z)}{\Delta T}, \tag{3.3}$$

the steady-state differential equations can be written in the form

$$[\mathrm{D}\mathrm{D}_* + \partial_z^2]^2 \psi_0 = -Re\left[\frac{2}{r}(\partial_z \psi_0) + (\mathrm{D}_* \psi_0)\,\partial_z - (\partial_z \psi_0)\,\mathrm{D}_*\right](\mathrm{D}\mathrm{D}_* + \partial_z^2)\,\psi_0 + \frac{Gr}{Re}\mathrm{D}\theta_0, \tag{3.4}$$

and

$$\frac{1}{RePr}(\mathrm{D}_* \mathrm{D} + \partial_z^2)\,\theta_0 = -\mathrm{D}_* \psi_0 - [(\mathrm{D}_* \psi_0)\,\partial_z - (\partial_z \psi_0)\,\mathrm{D}]\,\theta_0. \tag{3.5}$$

The solution of these equations must satisfy the boundary conditions

$$\psi_0 = \partial_z \psi_0 = \theta_0 = 0 \quad \text{on} \quad z = \pm\tfrac{1}{2}, \tag{3.6a–f}$$

and

$$\psi_0 = \mathrm{DD}_* \psi_0 - (\partial_z \psi_0 + 1) = (\mathrm{D} + B)\,\theta_0 = 0 \quad \text{on} \quad r = 1/\tilde{\Gamma}, \tag{3.7a–c}$$

where the characteristic scales used in (3.4)–(3.7) for lengths, velocities, and temperature are d, $Re\,\nu/d$, and ΔT, respectively. The aspect ratio is denoted by $\tilde{\Gamma} = d/R_0$ and the dimensionless surface tension Reynolds, Prandtl, Grashof, and Biot numbers are defined by

$$Re = \gamma d\,\Delta T/(\rho\nu^2), \tag{3.8}$$

$$Pr = \nu/\kappa, \tag{3.9}$$

$$Gr = g\beta\,\Delta T d^3/\nu^2, \tag{3.10}$$

$$B = hd/k. \tag{3.11}$$

The Marangoni number $Ma = RePr$ is often used by other authors in place of Re. The solution of the problem is expanded into complete radial and axial orthonormal functions

$$\psi_0 = \sum_{n=0}^{\infty} \sum_{m=1}^{\infty} \hat{\psi}^{(0)}_{nm}\, T_n(x)\, H_m(z), \tag{3.12}$$

$$\theta_0 = \sum_{n=0}^{\infty} \sum_{m=1}^{\infty} \hat{\theta}^{(0)}_{nm}\, T_n(x)\, R_m(z), \tag{3.13}$$

where $T_n(x)$ are Chebyshev polynomials. The axial harmonics $R_m(z)$ and Chandrasekhar functions $H_m(z)$ individually satisfy the corresponding boundary conditions (3.6a–f). They are given by

$$R_m(z) = \sqrt{2} \begin{cases} \sin(m\pi z), & m \text{ even} \\ \cos(m\pi z), & m \text{ odd}, \end{cases} \tag{3.14}$$

and

$$H_m(z) = \begin{cases} S_{m/2}(z), & m \text{ even} \\ C_{(m+1)/2}(z), & m \text{ odd}, \end{cases} \tag{3.15}$$

where

$$S_m(z) = \frac{\sinh \mu_m z}{\sinh \frac{1}{2}\mu_m} - \frac{\sin \mu_m z}{\sin \frac{1}{2}\mu_m}, \tag{3.16}$$

$$C_m(z) = \frac{\cosh \lambda_m z}{\cosh \frac{1}{2}\lambda_m} - \frac{\cos \lambda_m z}{\cos \frac{1}{2}\lambda_m}, \tag{3.17}$$

and the roots μ_m and λ_m satisfy

$$\coth \tfrac{1}{2}\mu - \cot \tfrac{1}{2}\mu = 0, \quad \tanh \tfrac{1}{2}\lambda + \tan \tfrac{1}{2}\lambda = 0. \tag{3.18a, b}$$

To determine the amplitudes $\hat{\psi}^{(0)}_{nm}$ and $\hat{\theta}^{(0)}_{nm}$, (3.4) and (3.5) are projected onto $H_l(z)$ and $R_l(z)$, respectively, by means of the scalar product $\int_{-\frac{1}{2}}^{\frac{1}{2}} \mathrm{d}z$. Since ψ_0 and θ_0 are coupled through the boundary condition (3.7b), the same method cannot be used radially, if the boundary conditions are to be satisfied exactly. Therefore, a Chebyshev–Tau method combined with the mapping

$$x = 2\tilde{\Gamma} r - 1 \tag{3.19}$$

is applied in the radial direction. The radial dependence is thus removed from the bulk equations by projecting them onto $T_k(x)$ using the standard Chebyshev weight. As ψ_0 has odd and θ_0 has even parity under inversion ($r \to -r$) we could have used odd and even Chebyshev polynomials separately on the interval $-1/\tilde{\Gamma} \leqslant r \leqslant 1/\tilde{\Gamma}$. The

reduced centre resolution of the latter method would be no disadvantage, since the basic flow and temperature fields are expected not to vary strongly in the vicinity of $r = 0$. However, we gave preference to the mapping, because one need not distinguish between even and odd functions and the introduction of different collocation points for the stability equations (see §4) can be avoided.

Given the axial and radial truncation orders M and N, $2M(N+1)$ algebraic equations for $\boldsymbol{\psi} = (\hat{\psi}^{(0)}_{nm}, \hat{\theta}^{(0)}_{nm})$ are obtained by projecting (3.4) onto $H_l(z)\,T_k(x)$ for $1 \leqslant l \leqslant M$ and $0 \leqslant k \leqslant N-4$, and projecting (3.5) onto $R_l(z)\,T_k(x)$ for $1 \leqslant l \leqslant M$ and $0 \leqslant k \leqslant N-2$. The remaining $6M$ equations are obtained from (3.7) and the requirement that the solution must be bounded on $r = 0$, i.e.

$$\psi_0 = \mathrm{D}\mathrm{D}_*\psi_0 = \mathrm{D}\theta_0 = 0 \quad \text{on} \quad r = 0. \tag{3.20a–c}$$

The boundary conditions (3.7*a*, *b*) and (3.20*a*, *b*) are projected onto $H_l(z)$, whereas (3.7*c*) and (3.20*c*) are projected onto $R_l(z)$. Collecting all equations the resulting set can be written in the form

$$\boldsymbol{A}\boldsymbol{\psi}_0 + \boldsymbol{N}(\boldsymbol{\psi}_0)\,\boldsymbol{\psi}_0 + \boldsymbol{K} = 0, \tag{3.21}$$

with

$$\boldsymbol{A} = \begin{bmatrix} A_{klnm} & B_{klnm} \\ D_{klnm} & E_{klnm} \end{bmatrix}, \quad \boldsymbol{N} = \begin{bmatrix} C_{klijnm}\,\hat{\psi}^{(0)}_{ij} & 0 \\ 0 & F_{klijnm}\,\hat{\psi}^{(0)}_{ij} \end{bmatrix}, \quad \boldsymbol{K} = \begin{bmatrix} \hat{K}_{kl} \\ 0 \end{bmatrix}, \tag{3.22a–c}$$

and where summation is over all pairwise indices. The driving force of the flow enters through the inhomogeneity $\boldsymbol{K}$, which results from the conducting temperature profile at the liquid surface entering boundary condition (3.7*b*). The coefficients A_{klnm}, B_{klnm}, D_{klnm}, E_{klnm}, C_{klijnm}, F_{klijnm}, and $\hat{K}_{kl}$ are given in an Appendix.† To solve (3.21) the Jacobian is calculated analytically and the solution is obtained by Newton–Raphson iteration.

4. Linear stability calculations

To investigate the hydrodynamic stability of the basic flow $\boldsymbol{u}_0 = (u_0, 0, w_0)$, p_0 and θ_0 we consider the temporal evolution of small disturbances $\boldsymbol{u} = (u, v, w), p$, and θ of the basic state on the diffusive timescale d^2/ν. Linearization of (2.1)–(2.3) with respect to the disturbance quantities yields

$$\partial_t \boldsymbol{u} + Re\,(\boldsymbol{u}\cdot\nabla\boldsymbol{u}_0 + \boldsymbol{u}_0\cdot\nabla\boldsymbol{u}) = -\nabla p + \nabla^2\boldsymbol{u} + \frac{Gr}{Re}\theta\boldsymbol{e}_z, \tag{4.1}$$

$$\nabla\cdot\boldsymbol{u} = 0, \tag{4.2}$$

$$\partial_t\theta + Re\,(w + \boldsymbol{u}\cdot\nabla\theta_0 + \boldsymbol{u}_0\cdot\nabla\theta) = \frac{1}{Pr}\nabla^2\theta. \tag{4.3}$$

The solution of these equations can be expanded into azimuthal normal modes

$$\begin{pmatrix} u \\ v \\ w \\ p \\ \theta \end{pmatrix} = \mathrm{e}^{\alpha t}\,\mathrm{e}^{\mathrm{i}\bar{m}\phi} \begin{pmatrix} \tilde{u}(r,z) \\ \tilde{v}(r,z) \\ \tilde{w}(r,z) \\ \tilde{p}(r,z) \\ \tilde{\theta}(r,z) \end{pmatrix} + \text{c.c.}, \tag{4.4}$$

† The Appendix is available, on request, from the authors or the Editorial Office.

where $\bar{m}$ is an integer azimuthal wavenumber, α a complex growth rate, and c.c. denotes the complex conjugate. To reduce the number of unknowns, p is eliminated by taking the curl of (4.1) and $\tilde{v}$ is removed with help of the continuity equation

$$\tilde{v} = -\frac{r}{\mathrm{i}\bar{m}}(\mathrm{D}_*\tilde{u} + \partial_z \tilde{w}), \quad \bar{m} \neq 0. \tag{4.5}$$

The reader is referred to the end of this section for the treatment of $\bar{m} = 0$. Written in components the following real system of equations for $\tilde{u}, \tilde{w}$, and $\tilde{\theta}$ is obtained from the r- and ϕ-components of the curl of (4.1) and equation (4.3):

$$\begin{aligned}\bar{m}^2[\partial_t - \nabla^2]\tilde{w} - r\left[\partial_t - \left(\nabla^2 - \frac{1}{r^2}\right)\right] r\partial_z(\mathrm{D}_*\tilde{u} + \partial_z\tilde{w}) + \frac{2\bar{m}^2}{r}\partial_z\tilde{u} \\ = \bar{m}^2\frac{Gr}{Re}\tilde{\theta} + Re\{-\bar{m}^2(\tilde{u}\partial_r + \tilde{w}\partial_z)w_0 - \bar{m}^2(u_0\partial_r + w_0\partial_z)\tilde{w} \\ + r\partial_z(u_0\partial_r + w_0\partial_z)r(\mathrm{D}_*\tilde{u} + \partial_z\tilde{w}) + r\partial_z(\mathrm{D}_*\tilde{u} + \partial_z\tilde{w})u_0\},\end{aligned} \tag{4.6}$$

$$\begin{aligned}\partial_t(\partial_z\tilde{u} - \partial_r\tilde{w}) - \partial_z\left(\nabla^2 - \frac{1}{r^2}\right)\tilde{u} + \partial_r\nabla^2\tilde{w} - \frac{2}{r}\partial_z(\mathrm{D}_*\tilde{u} + \partial_z\tilde{w}) \\ = -\frac{Gr}{Re}\partial_r\tilde{\theta} + Re\{\partial_r(\tilde{u}\partial_r + \tilde{w}\partial_z)w_0 + \partial_r(u_0\partial_r + w_0\partial_z)\tilde{w} - \partial_z(\tilde{u}\partial_r + \tilde{w}\partial_z)u_0 \\ - \partial_z(u_0\partial_r + w_0\partial_z)\tilde{u}\},\end{aligned} \tag{4.7}$$

and

$$(\partial_t - \nabla^2/Pr)\tilde{\theta} = -Re\{\tilde{w} + (\tilde{u}\partial_r + \tilde{w}\partial_z)\theta_0 + (u_0\partial_r + w_0\partial_z)\tilde{\theta}\}. \tag{4.8}$$

The solution of (4.6)–(4.8) must satisfy the axial boundary conditions

$$\tilde{u} = \tilde{w} = \partial_z\tilde{w} = \tilde{\theta} = 0 \quad \text{on} \quad z = \pm\tfrac{1}{2}, \tag{4.9a–h}$$

and the boundary conditions at the free surface resulting from (2.9)–(2.12)

$$\left.\begin{aligned} \partial_r\tilde{w} + \partial_z\tilde{\theta} &= 0 && (4.10)\\ \bar{m}^2\tilde{\theta} + (1/\tilde{\Gamma}^2)((\partial_r + \tilde{\Gamma})\partial_r\tilde{u} + \partial_r\partial_z\tilde{w}) &= 0 && (4.11)\\ \tilde{u} &= 0 && (4.12)\\ (\partial_r + B)\tilde{\theta} &= 0 && (4.13)\end{aligned}\right\} \quad \text{on} \quad r = \frac{1}{\tilde{\Gamma}}.$$

Since $\boldsymbol{u}$ and θ must be continuously differentiable at $r = 0$ we must demand (consider for example $\nabla\boldsymbol{u}$) that

$$\left.\begin{aligned} \tilde{u} = \partial_r\tilde{w} = \partial_r\tilde{\theta} = 0 \quad &\text{if} \quad \bar{m} = 0 && (4.14a–c)\\ \partial_r\tilde{u} = \tilde{w} = \tilde{\theta} = 0 \quad &\text{if} \quad \bar{m} = 1 && (4.15a–c)\\ \tilde{u} = \tilde{w} = \tilde{\theta} = 0 \quad &\text{if} \quad \bar{m} > 1 && (4.16a–c)\end{aligned}\right\} \quad \text{on} \quad r = 0.$$

The latter boundary conditions can be verified by Taylor expansion of $\boldsymbol{u}$ and θ around $r = 0$: $(\tilde{u}, \tilde{w}, \tilde{\theta}) \sim (r^{|\bar{m}-1|}, r^{\bar{m}}, r^{\bar{m}})$, $\bar{m} \geqslant 0$ (see also Xu & Davis 1984). Since the combined radial order of differential equations (4.6) and (4.7) is five, the total of five

radial boundary conditions for $\tilde{u}$ and $\tilde{w}$ is necessary and sufficient. The corresponding conditions on $\tilde{v}$ are always satisfied on the boundary, if $\bar{m} \neq 0$.

It is observed that (4.6)–(4.8) are invariant under inversion $r \to -r$, if either $\tilde{u}$ is even and $\tilde{w}$, $\tilde{\theta}$ are odd functions of r, or $\tilde{u}$ is odd and $\tilde{w}$, $\tilde{\theta}$ are even functions of r. Which case applies depends on the disturbance wavenumber $\bar{m}$ and can be determined from the asymptotic expansion of the differential equations for $r \ll 1$. This symmetry enables the calculation of the solution on the extended range $[-1/\tilde{\Gamma}, 1/\tilde{\Gamma}]$, thereby utilizing only even or odd Chebyshev polynomials. We do not follow this idea here; rather we proceed as in §3 and map the interval $r \in [0, 1/\tilde{\Gamma}]$ onto $x \in [-1, 1]$. The reason is that the utilization of these symmetries introduces the need for different collocation points for even and odd functions depending on $\bar{m}$ and that the corresponding computer program would be more involved. It turns out, moreover, that the neutral mode does vary in the bulk. Thus the number of collocation points near $r = 0$ should not be too small. Therefore, we expand

$$\begin{pmatrix} \tilde{u}(r,z) \\ \tilde{w}(r,z) \\ \tilde{\theta}(r,z) \end{pmatrix} = \sum_{n=0}^{\infty} \sum_{m=1}^{\infty} \begin{pmatrix} \hat{u}_{nm} R_m(z) \\ \hat{w}_{nm} H_m(z) \\ \hat{\theta}_{mn} R_m(z) \end{pmatrix} T_n(x), \tag{4.17}$$

using the same basis functions as in §3. For radial and axial truncation orders N and M the total number of unknowns is $3M(N+1)$. $3M(N+1)$-$7M$ equations are obtained by projecting all equations (4.6)–(4.8) onto $R_l(z)$ for $l \in [1, M]$ and onto $\delta(x_k)$ with Gauss–Lobatto collocation points

$$x_k = \cos(\pi(k+1)/N), \quad k \in [-1, N-1]. \tag{4.18}$$

Equations (4.6) and (4.8) are collocated at points with $k \in [0, N-2]$ while (4.7) is enforced at points $k \in [0, N-3]$. All equations obtained from collocation at x_{-1} and x_{N-1} and the equations obtained from projecting (4.7) onto $\delta(x_{N-2})$ are dropped in favour of those $7M$ equations that result from projection of the boundary conditions (4.11)–(4.13) and one set out of (4.14)–(4.16) onto $R_l(z)$, and projection of (4.10) onto $H_l(z)$. The resulting system of equations takes the form of a generalized eigenvalue problem

$$\alpha \begin{bmatrix} A^{11} A^{12} A^{13} \\ A^{21} A^{22} A^{23} \\ A^{31} A^{32} A^{33} \end{bmatrix}_{klnm} \boldsymbol{x} = \begin{bmatrix} B^{11} B^{12} B^{13} \\ B^{21} B^{22} B^{23} \\ B^{31} B^{32} B^{33} \end{bmatrix}_{klnm} \boldsymbol{x}, \tag{4.19}$$

where $\boldsymbol{x} = (\hat{u}_{nm}, \hat{w}_{nm}, \hat{\theta}_{nm})$ and the square matrices A^{ij} and B^{ij} given in the Appendix (see footnote on p. 000) are of order $M(N+1)$. Since the growth rate α does not appear in the boundary conditions, $7M$ rows of $A = A^{ij}$ are zero thus making A singular. The corresponding $7M$ infinite eigenvalues may be mapped onto some finite arbitrary ones (Goussis & Pearlstein 1989) or eliminated by reducing the system to a non-singular one of order $3M(N+1) - 7M$ (Gary & Helgason 1970; Peters & Wilkinson 1970). Although the mapping method requires less operations ($O(nk)$, n is the order of A and k is the number of infinite eigenvalues) as compared to the reduction method ($O(n^2 k)$), this advantage is more than compensated in the present case by the savings (cost is $O(n^3)$ operations) in inverting the reduced rather than the complete system. For that reason we employ the reduction method, which has also been used for a similar problem by Jones (1985*a*). Solving (4.19) this way, $(3N-4)M$ finite complex eigenvalues α_j are obtained, their values depending on the control parameters Re, Pr, Gr, $\tilde{\Gamma}$ and B. The hypersurface on which the maximum real part of these eigenvalues vanishes is the stability boundary.

Since the critical eigenvalues $\alpha_c = \pm i\omega_c$ and the corresponding eigenvectors $\boldsymbol{x}_c, \boldsymbol{x}_c^*$ appear as complex conjugate pairs, any neutral solution $f \in \{u, w, \theta\}$ has the structure

$$f(x, \phi, z, t) = \sum_{n=0}^{N} \sum_{m=1}^{M} R_m(z)\, T_n(x)\, e^{i\bar{m}\phi} [A_1 \hat{f}_{nm}\, e^{i\omega_c t} + A_2 \hat{f}_{nm}^*\, e^{-i\omega_c t}] + \text{c.c.}, \quad (4.20)$$

where A_i denotes arbitrary complex constants, the asterisk indicates complex conjugation, and $R_m(z)$ has to be replaced by $H_m(z)$ if $f = w$. Depending on A_1, A_2, and ω_c the supercritical flow and temperature will appear as a spatial mode ($\omega_c = 0$)

$$f = F(x, z) \cos(\bar{m}\phi + G), \quad (4.21)$$

as a travelling azimuthal wave ($\omega_c \neq 0$, one $A_i = 0$)

$$f = F(x, z) \cos(\bar{m}\phi \pm \omega_c t + G(x, z)), \quad (4.22)$$

or as a standing wave ($\omega_c \neq 0, |A_1| = |A_2| \neq 0$)

$$f = F(x, z) \cos(\bar{m}\phi) \cos(\omega_c t + G(x, z)). \quad (4.23)$$

The amplitude F and phase G (if $\omega_c \neq 0$) depend on the radial and axial coordinates. Nonlinear interactions determine the constants A_1 and A_2 and therefore the character of the supercritical oscillatory solution.

The procedure described above applies to bifurcations that break rotational invariance, i.e. $\bar{m} \neq 0$. However, the basic state might become unstable to axisymmetric ($\bar{m} = 0$) disturbances. This case has been treated by Shen *et al.* (1990). To include bifurcations to axisymmetric states in the present formalism with a minimum of changes, we observe that (4.7) and (4.8) can be used without modification even if $\bar{m} = 0$. Since the r-component of the curl of (4.1) vanishes, equation (4.6) is substituted by the continuity equation (4.2) and projected in the usual way. For $\bar{m} = 0$ boundary condition (4.11) must be dropped and radial collocation is now applied at all interior points x_k, $k \in [0, N-2]$. This method, in which continuity is only weakly satisfied, is a convenient extension. Its purpose is to check qualitatively whether or not $\bar{m} = 0$ can be the most dangerous mode.

5. Results and discussion

5.1. *Validation of the numerical procedure*

Reliable calculations for the two-dimensional base state are available in the literature. Therefore, the calculated basic state has been checked by comparison with a Stokes flow approximation for small Re and Pr (Kuhlmann 1989) and with nonlinear finite difference calculations of Shen *et al.* (1990). For small Re and Pr we found very good agreement with Kuhlmann (1989) even for a truncation order of $N = 16, M = 5$. Small deviations from the analytical solution occur only in the close vicinity of both corners. Agreement up to the thickness of a line has been obtained with the basic state streamfunction and temperature field calculated by Shen *et al.* (1990) for $Re = 1000, Pr = 0.01, B = 0.3$ and $\tilde{\Gamma} = 1$ (their figure 2*a*). For $Re = 10$ and $Pr = 10$, however, our result differs slightly from figure 2(*b*) of Shen *et al.* (1990). The largest deviation occurs in the radial derivative of the temperature field at the free surface. With heat loss included, $\partial_r \Theta(r = 1/\tilde{\Gamma})$ should be negative close to the cold corner, where $\Theta > 0$ (cf. (3.7*c*)), contrary to the obviously positive radial temperature gradient in their figure 2(*b*); ($\Theta = z + \theta_0$). For comparison our results are shown in figures 1 and 2. We note that the heat loss for $B = 0.3$ is so small that the negative

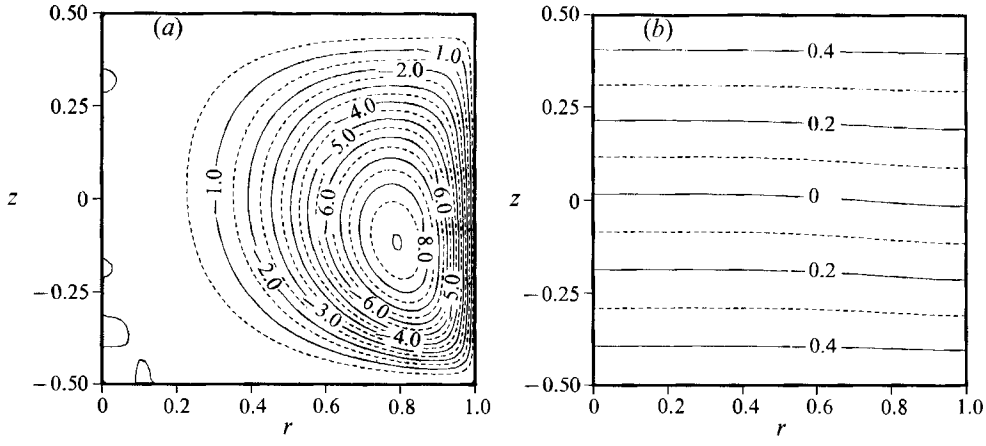

FIGURE 1. (*a*) Streamlines of the basic state $r\hat{\psi}_0 \times 10^3$, and (*b*) isotherms of the corresponding temperature field, for $Re = 1000$, $Pr = 0.01$, $Gr = 0$, $B = 0.3$, and $\tilde{\Gamma} = 1$.

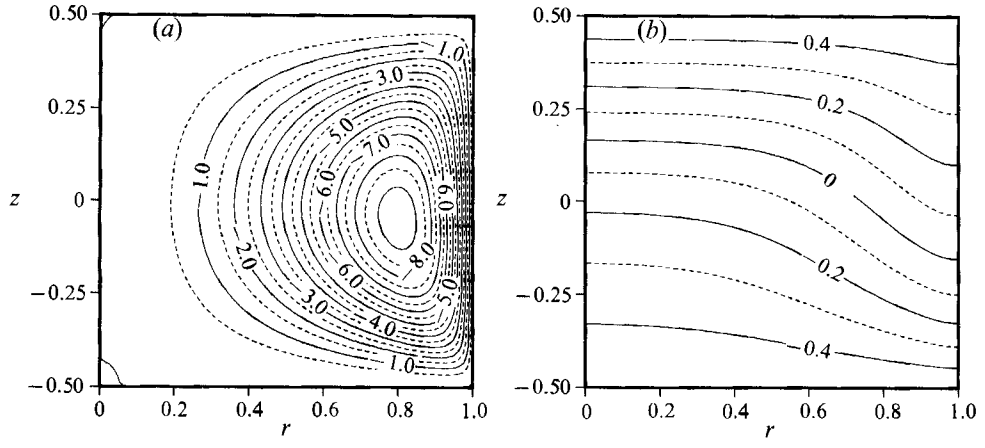

FIGURE 2. As figure 1, but $Re = 10$ and $Pr = 10$.

slope $\partial_r \Theta(r = 1/\tilde{\Gamma}) < 0$ is hardly noticeable in figures 1 and 2. A quantitative comparison shows that our value of $\psi_{\min} = -1.07 \times 10^{-2}$ for the streamfunction minimum for $Re = 100$, $Pr = 0.1$, $B = 0.3$, and $\tilde{\Gamma} = 1$ is only 2% smaller than the value given by Shen (1989) and 5% below that of Fu & Ostrach (1985).

Care has to be taken if the Marangoni number $Ma = RePr$ is so large that a steep axial temperature gradient is created at the cold corner. In this case an insufficient mode truncation in the axial direction can result in spatial oscillations of the truncated series (Gibbs phenomenon). It is this rapid variation of the fields at the cold corner that limits the accessible Prandtl number range. In figure 3 we show the energy conservation error at criticality (see further below) by comparing the total normalized heat flow through the boundary at $z = -\frac{1}{2}$ with the heat flow at $z = \frac{1}{2}$ for $B = 0$, i.e. for an insulating radial boundary. In this case both heat fluxes must be the same owing to energy conservation. The Nusselt number has been defined as $Nu = J^{\text{total}}/J^{\text{conductive}}$, where J is the total heat flow through the respective surface. The agreement between both Nusselt numbers is very good for $Pr < 1$. However, as Pr increases, the error gets larger and reaches 17% at $Pr = 20$. The reason is that at large Pr the heat flow through the cold boundary occurs mainly in a small area at

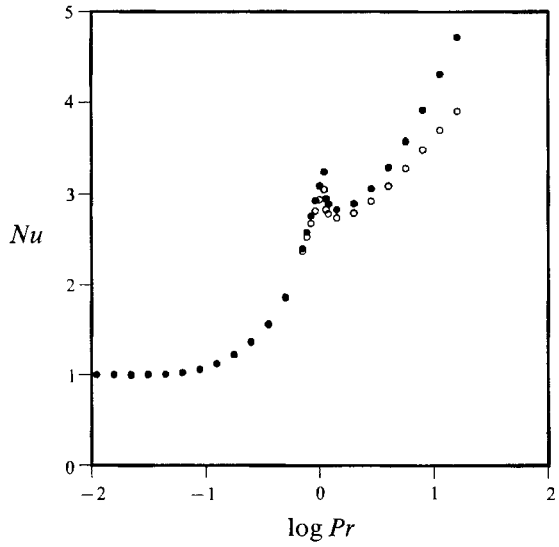

FIGURE 3. Nusselt numbers calculated for $z = 0.5$ (●) and $z = -0.5$ (○) at criticality for $\bar{m} = 1$, $Gr = 0$, $B = 0$, $\tilde{\Gamma} = 1$, $N = 16$, and $M = 12$.

$\tilde{\Gamma}$	$\bar{m}$	Ra_c Hardin *et al.* (1990)	$-Gr_c Pr$ present result
0.333	1	1768	1759
0.5	1	1832	1826
1.0	2	2470	2490
1.333	1	2592	2588
6.0	1	1.010×10^5	1.007×10^5

TABLE 1. Critical Grashof number for the onset of buoyant convection in a vertical cylinder. Comparison of the present critical values of $-Gr_c Pr$ for $N = 14$ and $M = 10$ with the corresponding critical Rayleigh number Ra_c obtained by Hardin *et al.* (1990). The value of Ra_c for $\tilde{\Gamma} = 1$ has been determined graphically from their figure 6.

$r = 1/\tilde{\Gamma}$. Since this region is most susceptible to truncation errors, the comparison of both Nusselt numbers is a very severe test, although Nu is an integral quantity. As will be discussed below, the instability mechanism for large Prandtl numbers is not very sensitive to the details of the corner flow and the convergence of the critical values with increasing truncation order is better than that of the energy conservation.

To test the general procedure a vertical cylindrical container with an insulating radial boundary heated from below was considered in the Boussinesq approximation. For a calculation of the linear stability boundary of the quiescent base state ψ_0 and θ_0 were set to zero and (4.10)–(4.11) were replaced by rigid boundary conditions $\tilde{w} = 0$ and $\partial_r \tilde{u} = 0$. The thermocapillary Reynolds number drops out of (4.1)–(4.3) and (4.6)–(4.8) by the appropriate scaling $\boldsymbol{u} \to \boldsymbol{u}/Re$ and $\theta \to \theta Pr$. The accordingly modified problem has been solved to obtain critical values of the Rayleigh number $Ra = -GrPr$, which are compared with high-precision linear stability boundaries of the quiescent base state given by Hardin *et al.* (1990). For a truncation of $N = 14$, $M = 10$, the present results listed in table 1 differ by less than 0.5% from those of Hardin *et al.* (1990).

These favourable comparisons prove the validity of most parts of the numerics.

	$N = 10$	$N = 12$	$N = 14$	$N = 16$
$M = 6$	0		348 (0)	348 (0)
	0		748 (0)	737 (0)
	0		521 (20.9)	516 (20.8)
$M = 8$		267 (0)	368 (0)	369 (0)
		137 (0)	749 (0)	763 (0)
		0	447 (21.4)	446 (21.3)
$M = 10$		259 (0)	364 (0)	366 (0)
		108 (0)	721 (0)	751 (0)
		0	425 (21.8)	425 (21.7)
$M = 12$				362 (0)
				742 (0)
				417 (22.0)

TABLE 2. Influence of the truncation order on the critical Reynolds number and oscillation frequency (in parentheses) for $\bar{m} = 1$, $Gr = 0$, and $B = 0$. Consecutive numbers are given for $Pr = 0.0078$, 0.25, and 4.0.

However, the buoyancy-induced instability in a vertical cylinder is a smoother problem than that of thermocapillary convection. This is because the thermocapillary basic state can exhibit strong spatial variations in contrast to the trivial base state for the heated cylinder problem ($Re = 0$). For that reason the effect of different truncation orders on the stability boundary was calculated for selected cases (table 2). To get a reasonable stability boundary, the radial truncation order N must be sufficiently large, e.g. for truncation orders of $N < 14$ the values for the stability boundary have not yet converged, especially for large Prandtl numbers. This might have to do with the appearance of boundary layers below the free surfaces (see further below), which cannot be resolved for too low truncation orders. The axial truncation order M does not have such a dramatic effect on the stability boundary. Therefore, slight axial waviness of the solution does not significantly influence the integral property Re_c. For all the following calculations we used a truncation of $N = 16$ and $M = 12$ and estimate the relative error of Re_c for $\bar{m} = 1$ to be about 1–10% depending on Pr. Unless mentioned otherwise an aspect ratio of $\tilde{\Gamma} = 1$ is considered in the following.

5.2. *The Prandtl number dependence of the linear stability boundary and the structure of the neutral modes*

The dependence of the linear stability boundary of the steady base state on the Prandtl number was determined in the following way. The basic state was calculated for a small Reynolds number using a Stokes flow approximation (Kuhlmann 1989) as an initial guess. By a stepwise increase of the Reynolds number the basic solution was then traced to larger values of Re. If the stability analysis, which was performed for each Reynolds number after convergence of the respective base state, indicated a change of sign of the real part of the eigenvalue considered, the zero of the growth rate was detected by the secant method or by subdivision of intervals. After that, the Prandtl number was changed in small steps and the above procedure was used to determine the new stability boundary starting with the previously calculated base state as the initial guess.

Neutral curves of the most dangerous modes for wavenumbers $\bar{m} = 1$ and 2 are shown in figure 4(*a*). Both curves have a similar shape. Of these modes, $\bar{m} = 1$ is the

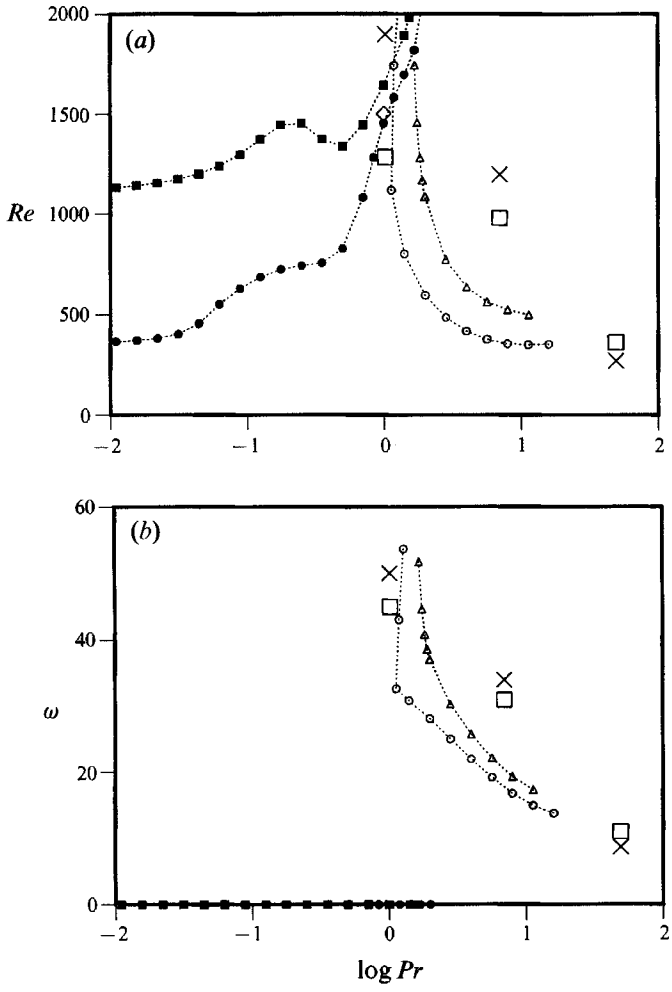

FIGURE 4. (*a*) Neutral curves for $\bar{m} = 1$ (●, ○) $\bar{m} = 2$ (■, △), $Gr = 0$, and $B = 0$. The critical Reynolds number is shown as function of the logarithm of the Prandtl number. (*b*) Hopf frequency ω_c of the neutral solution. Crosses and open squares are experimental values of Velten *et al.* (1991) obtained for liquid bridges heated from below and above, respectively. The diamond is the energy stability limit ($\bar{m} = 1$) obtained by Neitzel *et al.* (1991). The dotted lines are guides to the eye.

most dangerous one. Each neutral curve consists of two different branches. For $Pr < 1$ the basic state looses its stability to a stationary disturbance corresponding to the spatial mode (4.21) and the supercritical flow has the shape of a tilted ($\bar{m} = 1$) or quenched ($\bar{m} = 2$) torus. For larger Prandtl numbers the instability is oscillatory with Hopf frequencies ω_c given in figure 4(*b*). Here, the neutral solution is a superposition of two counter-propagating waves in the azimuthal direction according to (4.22) and (4.23). The sharp increase of ω_c for $\bar{m} = 1$ as $Pr \downarrow 1$ is not a discontinuity but a continuous change due to the strong turning of the stability boundary.

The appearance of these different neutral branches must be related to different instability mechanisms. The critical value $Re_c(\bar{m} = 1) = 362$ for $Pr = 0.0078$ is very close to the limiting value for vanishing Prandtl number ($Re_c(\bar{m} = 1, Pr = 10^{-6}) = 356$). By taking this limit, the disturbance equation (4.8) reduces to a Laplace

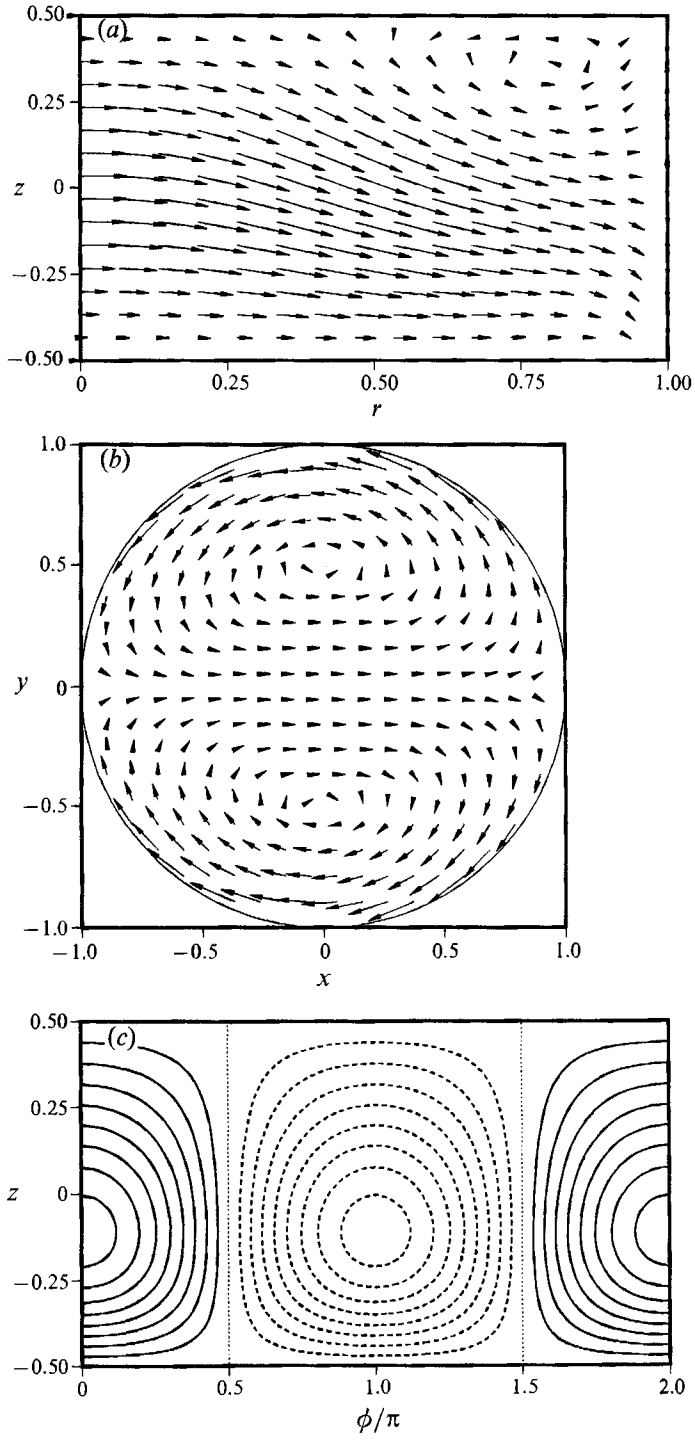

FIGURE 5. Neutral mode for $Pr = 0.0078$, $Gr = 0$, and $B = 0$. (*a*) Velocity field in a radial cut at $\phi = 0$, (*b*) velocity field in a horizontal cut at $z = -0.3$, and (*c*) surface temperature distribution.

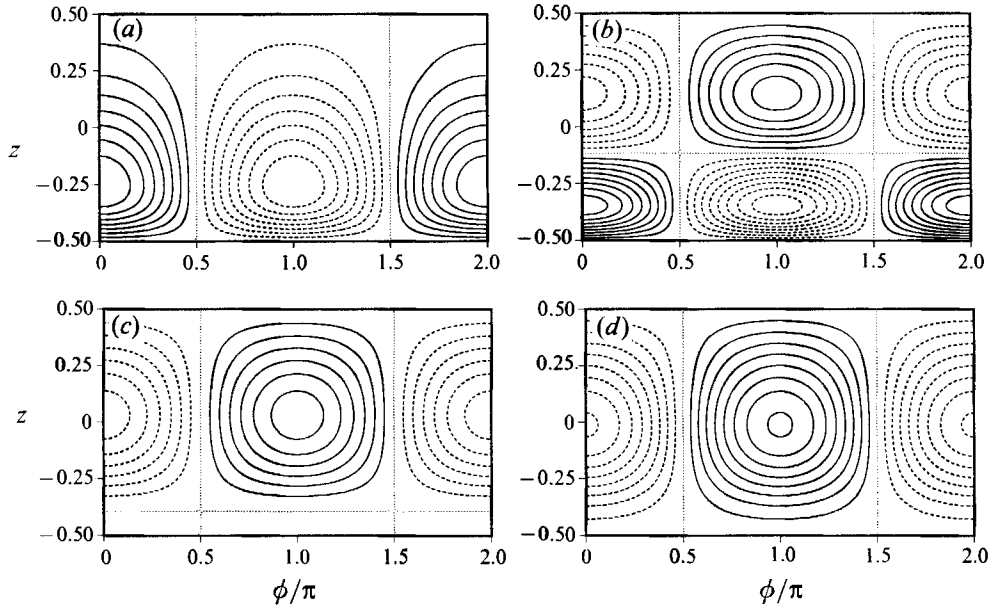

FIGURE 6. Surface temperature distribution of the neutral mode for $Gr = 0$, $B = 0$, and (*a*) $Pr = 0.088$, (*b*) $Pr = 0.125$, (*c*) $Pr = 0.177$, and (*d*) $Pr = 0.250$.

equation for $\tilde{\theta}$. Its solution for the homogeneous boundary conditions given in (4.9), (4.13) and (4.14)–(4.16) is $\tilde{\theta} = 0$. Since $B \to 0$ for $Pr \to 0$ and h finite, the same equation and boundary conditions also govern θ_0. Therefore, the complete temperature field is given by $\theta = \theta_0 = 0$ independent of $T_a(z)$ and no thermocapillary forces can act except for the constant shear stress ($DD_* \psi_0 = 1$) that is driving the basic flow field. Any instability that persists for $Pr \to 0$ at finite Reynolds number must necessarily be hydrodynamic in nature. Consequently, the use of the Reynolds number instead of the Marangoni number is appropriate for small Prandtl numbers.

The small-Pr instability breaks the axisymmetry. Such hydrodynamic symmetry-breaking bifurcations have also been observed in other systems, for instance the breaking of mirror symmetry in very short Taylor vortex annuli (Barten, Lücke & Kamps 1990) or the breaking of axisymmetry in the transition from Taylor vortex flow to modulated vortex flow (Jones 1985*b*). A stationary thermocapillary flow with broken axisymmetry has also been found by Rupp *et al.* (1989) to exist in cylindrical liquid bridges prior to the onset of time-dependent flow.

Figure 5(*a–c*) illustrates the critical disturbance flow pattern for $Pr = 0.0078$, $Re_c = 362$, $Gr = 0$, and $B = 0$. In the interior of the liquid bridge the disturbance flow is mainly unidirectional, where the inward flow has a positive $\tilde{w}$-component and the outward flow has a negative $\tilde{w}$-component. Mass conservation forces this flow to split into two opposite azimuthal jets at $r = 1/\tilde{\Gamma}$ and $\phi = 0$, which establish a return flow in a small area close to the cold corner and which merge at $\phi = \pi$. Because the basic temperature field for small Pr (figure 1*b*) depends essentially on z only, the descending radial outward flow (figure 5*a*) transports hot fluid from the upper bulk to the surface at $\phi = 0$ and produces a hot surface spot. A corresponding cold spot is generated at $\phi = \pi$ (figure 5*c*). Azimuthal thermocapillary effects support this motion; however, they are insignificant at this low Marangoni number.

By increasing Pr the basic state develops radial temperature gradients and the temperature of the fluid transported to the free surface by radial disturbance flow

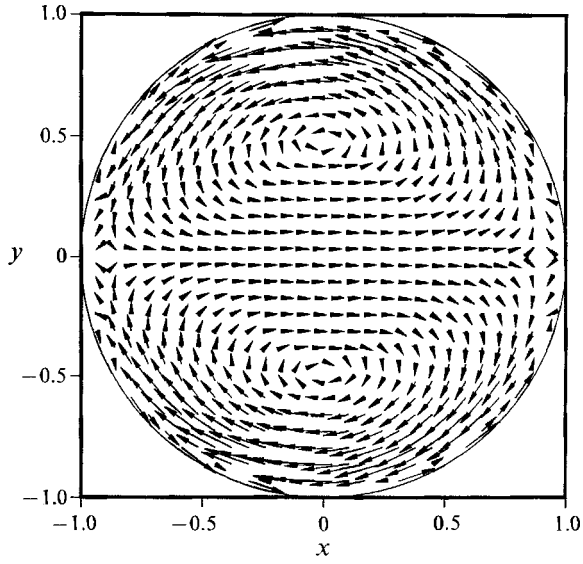

FIGURE 7. Neutral flow field in a horizontal cut at $z = -0.15$ for $Re_c = 825$, $Pr = 0.5$, $Gr = 0$, and $B = 0$. Note the thin surface layer in which the velocity is opposite to the bulk flow.

can be lower than the basic state temperature at the surface. In this way a cold spot is generated in addition to the hot spot at $\phi = 0$. It first appears at the hot end at $z = \frac{1}{2}$ for $Pr \approx 0.1$. For even larger Prandtl numbers this cold spot on top of the hot one becomes larger at the expense of the hot spot, which finally vanishes at $Pr \approx 0.2$. A neutral surface disturbance temperature sequence illustrating this behaviour is shown in figure 6(*a–d*). For still larger Prandtl numbers azimuthal thermocapillary forces become more effective, suppressing the disturbance flow from the cold spot to the hot spot. Although the basic state also depends on Pr with correspondingly altered stability properties, the azimuthal thermocapillary forces alone can explain the stabilization of the basic state, if the Pr number is increased. If thermocapillarity were solely responsible for the low Pr instability, a complete stabilization could have been expected for cases in which the radial outward flow is associated with a cold spot like in the classical Marangoni problem (Pearson 1958). A total suppression of the instability, however, is not observed, giving further evidence for the hydrodynamic origin of the instability. Instead, for $Pr = O(1) < 1$ the azimuthal return flow takes place in a thin shear layer in which the azimuthal velocity changes sign. It is directed toward the cold spot at the surface, whereas it is directed away from it just below a thin surface layer. An example is shown in figure 7 for $Pr = 0.5$. Here the boundary-layer thickness is $\approx 0.06/\tilde{\Gamma}$. With the smallest distance between adjacent collocation points being $\approx 0.01/\tilde{\Gamma}$, three collocation points including one boundary point lie within the shear layer, which proves that the appearance this boundary layer is physical and not a numerical artifact.

At about $Pr = 1$ the low-Pr stability boundary intersects with another neutral branch enclosing a codimension-two point. This large-Pr branch has been followed up to $Pr \approx 20$. All neutral modes have the same character along this curve. Since this instability branch is distinct from that for small Pr, another mechanism must be responsible for it. For large Pr the basic state develops a strong axial shear flow with strong radial temperature gradients below the free surface (the hotter fluid being closer to it). Under these conditions one is expecting hydrothermal wave instabilities

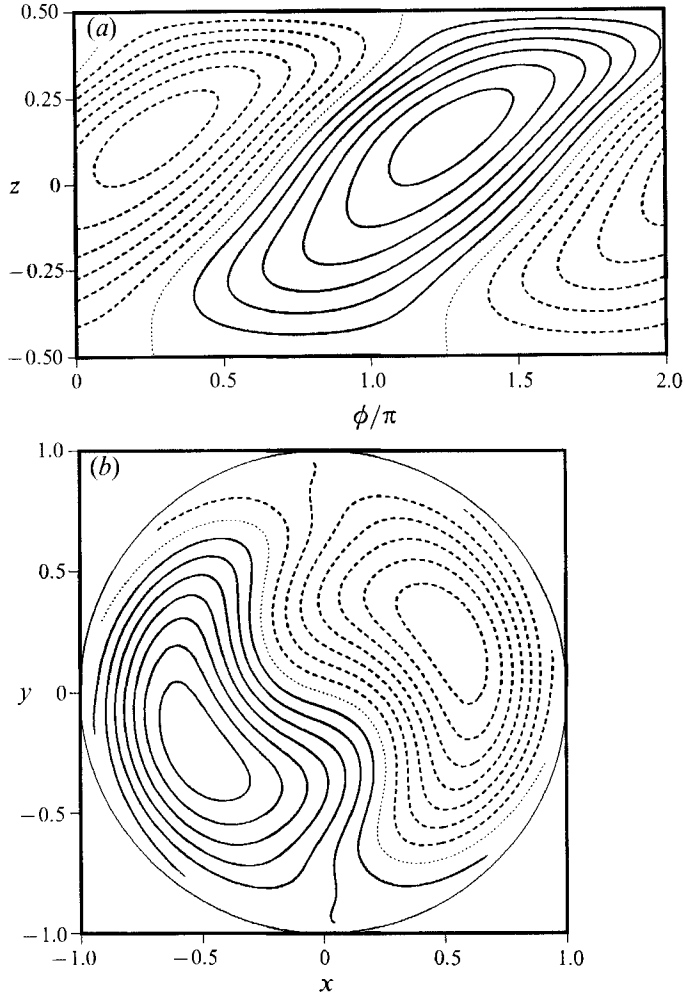

FIGURE 8. Critical disturbance temperature field at $Re_c = 595$, $Pr = 2$, $Gr = 0$, and $B = 0$: (*a*) azimuthal cut at $r = 0.75/\tilde{\Gamma}$, (*b*) horizontal cut at $z = 0$.

as described by Smith (1986*b*). The streamwise surface temperature gradient present in the analysis of Smith & Davis (1983*a*) was required to generate the flow, but is not present here at midgap, since the streamwise temperature gradients are located at the corner regions (cf. Carpenter & Homsy 1990). Note that this temperature gradient is not important for the high-Pr instability mechanism given by Smith (1986*b*). In fact we find that the supercritical flow is a superposition of two hydrothermal waves. Both waves propagate upstream of the surface flow at a certain angle with respect to the vertical axis. This description is equivalent to two azimuthal waves propagating in opposite directions and having inclined wave fronts. Mathematically this is expressed by a non-zero phase $G(x, z)$ in (4.22). The isotherms of a typical wave propagating in the negative ϕ-direction are shown in figure 8(*a*) along an azimuthal cut at $r = 0.75/\tilde{\Gamma}$ for $Re = Re_c = 595$, $Pr = 2$, $Gr = 0$, $B = 0$, and $\tilde{\Gamma} = 1$. As in Smith (1986*b*) we find large temperature maxima (minima) in the interior of the liquid bridge propagating ahead of the respective surface maxima (minima) and conductively heating (cooling) them. This is demonstrated in figure 8(*b*), where the corresponding isotherms are shown in a horizontal cut at $z = 0$. The

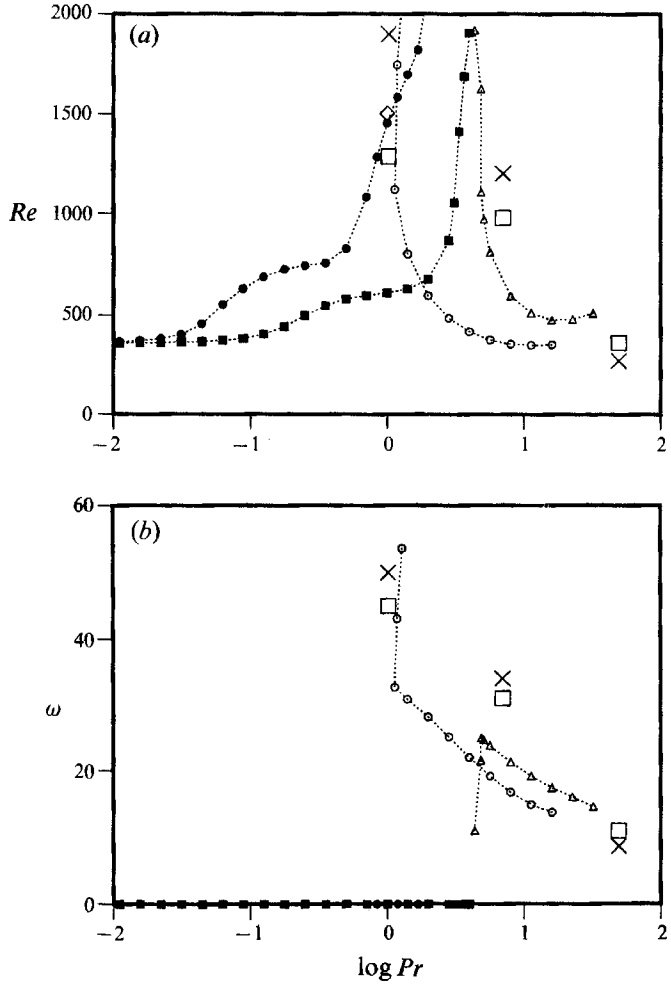

FIGURE 9. (*a*) Critical curves Re_c versus log (Pr) for $\bar{m} = 1$ and $B = 0$ (●, ○) and $B = 10$ (■, △). (*b*) Corresponding circular frequencies ω_c of the neutral mode. Crosses, open squares, and diamond as in figure 4.

details of the corner flow are only important in so far as they determine the strength of the surface flow, but they do not directly influence the large-Pr instability, which is triggered in the midgap area where the largest radial gradients of the axial velocity and the temperature occur.

5.3. *The influence of heat loss*

Heat transfer from the liquid bridge to its surroundings is modelled by (3.7*c*), where it has been assumed that the external temperature is equal to the conducting profile. The effect of cooling on the base-state stability is demonstrated in figure 9 for wavenumber $\bar{m} = 1$ by comparing the stability boundary for $B = 10$ (solid squares and triangles) with that for an insulating surface ($B = 0$, dots and circles). The gross effect of heat loss is to shift the stability boundary towards larger Prandtl numbers. The same qualitative behaviour is also found for $\bar{m} = 2$. The Hopf frequencies of the hydrothermal waves generally increase with increasing heat loss except for those Pr

where the slope of Re_c versus Pr gets extremely large and the neutral curve takes an s-shaped form. Here, ω_c decreases continuously for critical Reynolds numbers larger than Re_c at the inflexion point of the neutral curve.

Heat loss at the interface affects both the base state and the disturbances. In the small-Pr regime heat loss reduces the radial temperature gradients of the basic state. This shifts the Prandtl number region, where the hot spot associated with radial outward flow turns into a cold spot, to larger values of Pr. Likewise, the stabilization, i.e. the suppression of the azimuthal jets by counter-acting thermocapillary forces, is reduced. Thus the influence of heat loss on the base state is destabilizing, if Pr is small. If Pr is less than $Pr \approx 0.1$, the hot spot corresponding to the radial outflow is cooled and the disturbance is reduced, which corresponds to a stabilization. On the other hand the suppression of the cold spot by heat loss for $Pr > 0.2$ corresponds to a destabilization. We observe (figure 9a) that for $B = 10$ the total effect is always destabilizing. In the limit of $B \to \infty$ the stationary instability branch should reach the hydrodynamic limit of $Re_c \approx 356$ for all Pr numbers.

Smith & Davis (1983a) showed that the base state is stabilized to hydrothermal waves when the Biot number is increased. This effect is solely due to the heat loss of the disturbance, since the base state considered was independent of B. In the present liquid bridge the influence of heat loss on the fully developed basic state at larger Pr is not trivial. But large heat loss will generally reduce the radial temperature gradients and the strength of the surface shear flow so that the disturbances cannot extract as much energy from the basic state as for $B = 0$. Therefore, the base state is always stabilized to hydrothermal waves by an increase of the Biot number, when Pr is large.

5.4. *The effect of weak buoyancy forces*

Frequently, buoyancy is considered a disturbing effect when thermocapillary flows are studied. In this case, i.e. for weak buoyancy forces, we have not found any multiplicity of the two-dimensional basic flow state (for $Gr = 0$ we have implicitly assumed that the base state is unique). However, if destabilizing buoyancy forces dominate the base flow in the bulk of the liquid, two different axisymmetric basic states can arise, which correspond to either up- or downflow at the centreline. Here we consider only bifurcations from a basic state, which is dominated by thermocapillary convection.

Many experiments have been carried out using small volumes of liquid to reduce the Grashof number. For a given geometry and in the Boussinesq approximation the ratio Gr/Re is a constant when ΔT is varied experimentally to control Re. Typically, this constant is of the order of one. Stability boundaries corresponding to this restriction are shown in figure 10(a, b) for $Gr = 0$ (dots), $Gr = Re$ (circles), and $Gr = 2Re$ (triangles). These positive values of the Grashof number correspond to heating from above in our notation. No qualitative change in the stability boundaries can be observed and in general the basic state is stabilized to a degree, which corresponds to the magnitude of Gr, as intuition suggests. The critical oscillation frequencies ω_c of the hydrothermal waves for $Pr > 1$ are slightly increased under the action of stabilizing buoyancy. Since $Gr \propto Re$, the stabilization is most pronounced for the largest critical Reynolds numbers, i.e. for $Pr \approx 1$.

Results for fixed Grashof numbers $Gr = \pm 2000$ are given in figure 11(a, b). The stability curve for $Gr = 0$ is shifted to smaller values of Re_c for systems heated from below (triangles) and to larger values of Re_c if heated from above (circles). An exception is found only for large Pr, where the neutral curve for $Gr = -2000$ has a minimum at about $Pr \approx 4$. This peculiar behaviour is related to the fact that for fixed

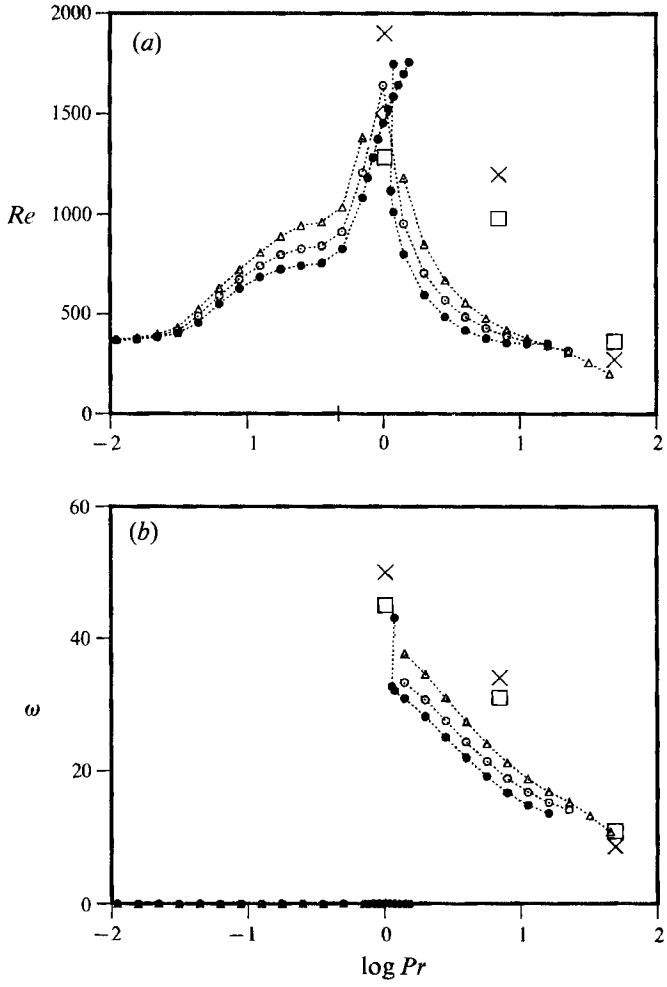

FIGURE 10. (*a*) Neutral curves and (*b*) Hopf frequencies for $\bar{m} = 1$, $B = 0$, and $Gr = 0$ (●), $Gr = Re$ (○), and $Gr = 2Re$ (△). Crosses, open squares, and diamond as in figure 4.

Gr the Rayleigh number Ra increases linearly with Pr so that the flow may well be three-dimensional even for $Re = 0$. We found, for instance, that the quiescent base state ($Re = 0$, $Gr = -2000$) is unstable to $\bar{m} = 1$ disturbances if $Pr > Pr^* = 1.136$ corresponding to $Ra_c(\bar{m} = 1) = 2272$. The study of the different bifurcation branches for buoyancy-dominated flows close to the axis $Re = 0$ is, however, beyond the scope of the present investigation. Therefore, the stability boundary Re_c given as triangles in figure 11 for destabilizing buoyancy forces does not guarantee that the two-dimensional flow is linearly stable for all Reynolds numbers $Re < Re_c$, especially if the Prandtl number is large and $Re \ll Re_c$. It should be noted that both the equations for the two-dimensional base state and those for the three-dimensional disturbances are invariant under the transformation $(Re, z, u^{(0)}, \theta^{(0)}, \tilde{u}, \tilde{\theta}) \rightarrow (-Re, -z, -u^{(0)}, -\theta^{(0)}, -\tilde{u}, -\tilde{\theta})$ even for $Gr \neq 0$. Accordingly, all neutral curves are symmetric with respect to the line $Re = 0$.

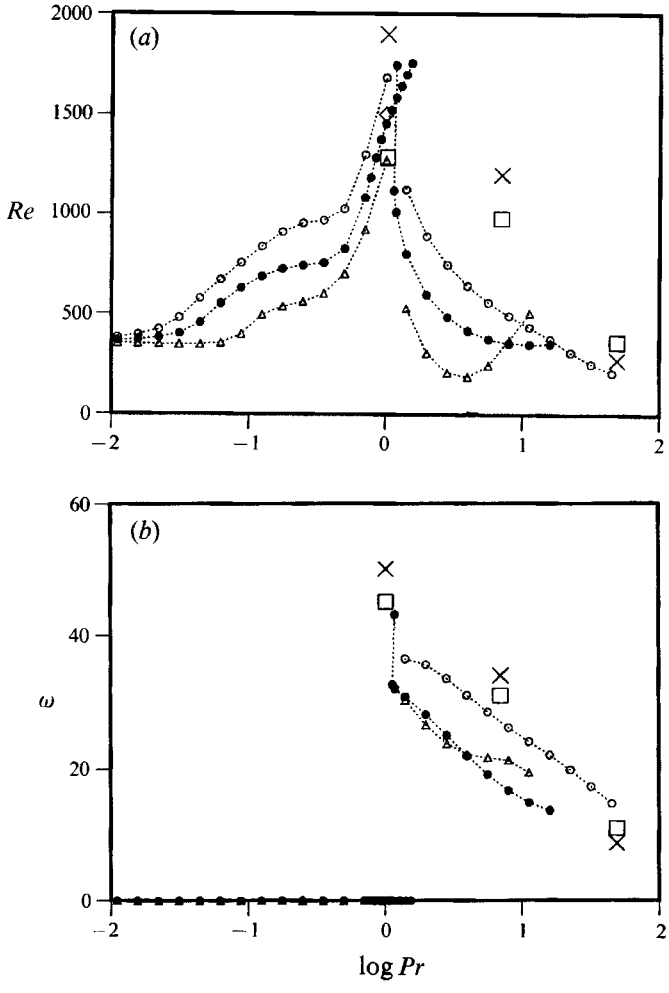

FIGURE 11. (*a*) Neutral curves and (*b*) Hopf frequencies for $\bar{m} = 1$, $B = 0$, and $Gr = 0$ (●), $Gr = 2000$ (○), and $Gr = -2000$ (△). Crosses, open squares, and diamond as in figure 4.

5.5. *The influence of the aspect ratio on the stability boundary*

The critical Reynolds number for the onset of thermocapillary convection with wavenumber $\bar{m} = 1$ is shown in figure 12 for $Pr = 0.0078$, $B = 0$, and $Gr = 0$ (dots) as function of various aspect ratios around $\tilde{\Gamma} = 1$ together with the neutral curve for $\bar{m} = 2$ (circles). The critical curve for $\bar{m} = 1$ shows a marked minimum at about $\tilde{\Gamma} \approx 1.1$ ($Re_c = 350$) and increases sharply for smaller and larger aspect ratios, while the neutral curve for $\bar{m} = 2$ increases monotonically with $\tilde{\Gamma}$. The behaviour for large $\tilde{\Gamma}$ is expected, since in the limit $Pr \to 0$ and $\tilde{\Gamma} \to \infty$ the basic flow approaches cylindrical Poiseuille flow, which is linearly stable at any Reynolds number. The observed stabilization of the $\bar{m} = 1$ mode for $\tilde{\Gamma} \to 0$ on the other hand is analogous to the behaviour found experimentally by Preisser *et al.* (1983), though for larger Prandtl numbers. They showed that the critical wavenumber increases monotonically with decreasing aspect ratio, whereas the critical Reynolds number does not change much. This implies an increasing linear stability boundary for the low-wavenumber disturbances. Our calculations for $Pr = 4$ confirm this behaviour (figure 13*a*). Here,

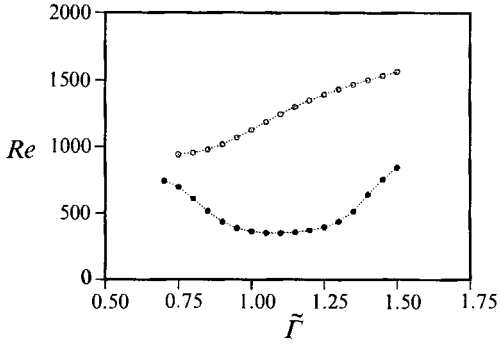

FIGURE 12. Neutral stability curves versus $\tilde{\Gamma}$ for $\bar{m} = 1$ (●) and $\bar{m} = 2$ (○), $Pr = 0.0078$, $Gr = 0$, and $B = 0$.

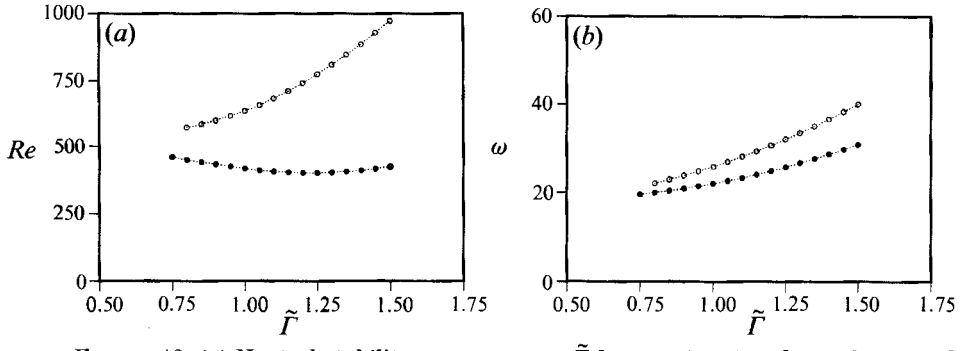

FIGURE 13. (*a*) Neutral stability curves versus $\tilde{\Gamma}$ for $\bar{m} = 1$ (●) and $\bar{m} = 2$ (○) and (*b*) corresponding Hopf frequencies. $Pr = 4.0$, $Gr = 0$, and $B = 0$.

the minimum of $Re_c(\bar{m} = 1) = 401$ ($\omega_c = 25$) is only weak and occurs at $\tilde{\Gamma} \approx 1.23$. The neutral curve for $\bar{m} = 2$ has a large positive slope and possibly intersects with the $\bar{m} = 1$ curve at an aspect ratio $\tilde{\Gamma} < 0.75$. The corresponding Hopf frequency curves shown in figure 13(*b*) increase monotonically with $\tilde{\Gamma}$. It is seen from figures 12 and 13 that the neutral curves for $\bar{m} = 1$ and $\bar{m} = 2$ show the same qualitative dependence on the aspect ratio for both the stationary and the oscillatory neutral branches. This indicates the major role of geometry in the pattern selection process for thermocapillary convection.

6. Comparison with previous work

A comparison of the present results for a finite-size liquid bridge with those obtained by Xu & Davis (1984) for an infinitely long liquid bridge shows that end effects are important. They introduce new instability mechanisms that are absent in the infinite case. The small-Prandtl-number hydrodynamic instability is not present in the bulk of a long liquid bridge, since the assumed Poiseuille flow is linearly stable for all Reynolds numbers, and it was shown that the critical Reynolds number diverges in the infinite case as $Pr \to 0$. Although spiral hydrothermal waves with wavenumber $\bar{m} = 1$ are the most dangerous disturbances in both finite and infinite liquid cylinders for a certain range of Prandtl numbers larger than $Pr = 1$ (depending on B), these are propagating downstream of the surface flow in the infinitely long system while they are propagating upstream in the present case as they also do in plane thermocapillary liquid layers. A critical axisymmetric oscillating state or propagating wave, present in the infinite system for very large Prandtl numbers, has

not been detected within the considered Pr range in the present analysis of a finite liquid bridge.

The diamond plotted in figure 4 indicates the energy stability limit of Neitzel *et al.* (1991) for $Pr = 1$, $B = 0.3$, $Gr = 0$, and $\bar{m} = 1$. Since the small but finite value of the heat loss parameter $B = 0.3$ leads to only a weak destabilization of the base state as compared to $B = 0$, the difference between the given energy limit of $Re^{\text{Energy}} = 1503$ and the present linear theory $Re_c = 1450$ is within the numerical tolerance. This result can be considered as another confirmation of the present theory, because experiments have shown that the first instability is non-hysteretic, in which case the proper energy limit may coincide with the linear stability boundary similar as, for example, for the heated cylinder problem, cf. Shen *et al.* (1990). The linear stability analysis of Neitzel *et al.* (1992) for the same problem yielded a much larger critical Reynolds number ($Re_c = 2484$) and also a different critical mode ($\bar{m} = 2$). This difference might be because the latter authors anticipated a Hopf bifurcation rather than a stationary instability. In fact, from figure 4 it is seen that the oscillatory instability branch for $\bar{m} = 1$ turns back just before crossing $Pr = 1$.

To date experiments have been exclusively designed to detect the onset of time-dependence rather than the onset of three-dimensionality of the flow. This is one of the reasons why the hydrodynamic stationary instability for $Pr < 1$ has not yet been observed experimentally. Most of the model experiments have been carried out with fluids of $Pr > 1$. Some recently determined stability boundaries and oscillation frequencies (Velten *et al.* 1991) have been included in figures 4 and 9 as squares and crosses. Since the linear stability boundary to oscillatory perturbations varies very strongly with Prandtl number and heat transfer conditions if $Pr = O(1)$, even slight uncertainties in Pr or in the heat transfer can significantly influence the critical Reynolds number. In this context the order of magnitude agreement between theory for $B = 0$ and experiment for $Pr = 1$ must be considered fortuitous. More obviously, the theory for $B = 0$ does not agree with the experimental results for $Pr = 7$. Apart from the free-surface deformability this difference can be attributed to the large heat loss of the liquid bridge in the experiments with $NaNO_3$ ($Pr = 7$). From figure 3 of Preisser *et al.* (1983) a Biot number of $B \approx 7$ can be estimated. Including heat loss ($B = 10$) diminishes the discrepancy for $Pr = 7$ considerably. Note, however, that the idealized heat transfer law employed (equation (2.12)) is only a phenomenological approximation and a detailed comparison would require the calculation of the exterior flow and temperature fields. A similar heat loss as for $Pr = 7$ was also present in the experiments with KCl ($Pr = 1$). Since weak buoyancy effects inside the liquid bridge could not have qualitatively influenced the transition to hydrothermal waves (see figure 10), it is very likely that the onset of oscillations in the latter experiment was due to a secondary instability.

The large and counter-intuitive difference in the critical Reynolds number – heated from below is more stable than heated from above – in the experiments for $Pr = 1$ and 7 can be explained by a heat loss that depends on the direction of gravity. If the liquid bridge is heated from above a weak eddy is driven by the thermocapillary flow in the surroundings, since the buoyant exterior flow is directed upward. This eddy separates the rising cold air from the free surface and reduces the heat loss as compared to the case when the liquid zone is heated from below. This way the basic state is stabilized to oscillatory disturbances such that the stabilization is most pronounced if the liquid is heated from below (Velten *et al.* 1991).

It has been shown that steady two-dimensional thermocapillary convection is quite stable to axisymmetric disturbances (Shen *et al.* 1990). This is confirmed by the

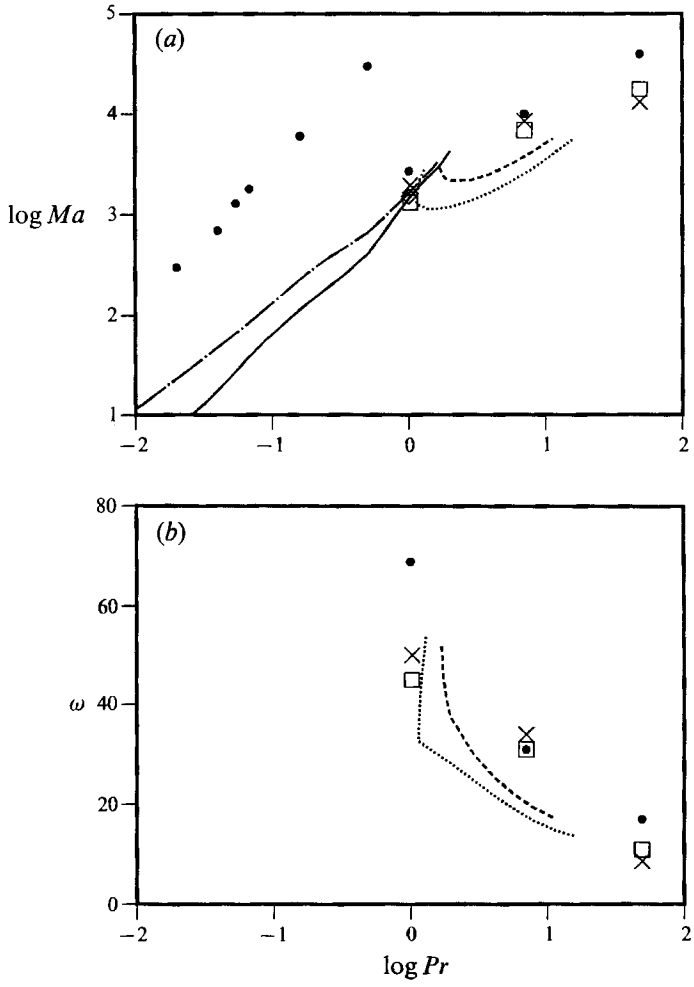

FIGURE 14. (*a*) Critical Marangoni number $Ma_c = Re_c Pr$ and (*b*) Hopf frequency as a function of the Prandtl number for $Gr = 0$, $B = 0$, and $\tilde{\Gamma} = 1$: ——, $\bar{m} = 1$, $\omega_c = 0$; —·—·—, $\bar{m} = 2$, $\omega_c = 0$; · · · ·, $\bar{m} = 1$, $\omega_c \neq 0$; – – –, $\bar{m} = 2$; $\omega_c \neq 0$. Squares, crosses, and diamond as in figure 4. The dots are transition points from steady three-dimensional to oscillatory flow for $\bar{m} = 2$ and $\tilde{\Gamma} = 1.2$ given by Rupp *et al.* (1989).

present study and it is also in agreement with earlier experimental observations (Preisser *et al.* 1983). In the majority of their recent experiments Velten *et al.* (1991) observed that the stability of the steady state is lost to a mode travelling in the axial direction while the phase also depends on the azimuth. This mode was named a 'mixed mode'. It can be readily explained as a superposition of two counter-propagating hydrothermal waves with equal amplitudes, the general form of which is (4.23). The appearance as an axially travelling wave with a ϕ-dependent wave fronts results from the phase front inclination of the hydrothermal waves.

As a comparison with results of other authors we show in figure 14 the critical Marangoni number as function of the Prandtl number, both on the usual logarithmic scale. Dots indicate transition points to time-dependent flow with $\bar{m} = 2$ obtained for $\tilde{\Gamma} = 1.2$ by Rupp *et al.* (1989) during a three-dimensional numerical simulation.

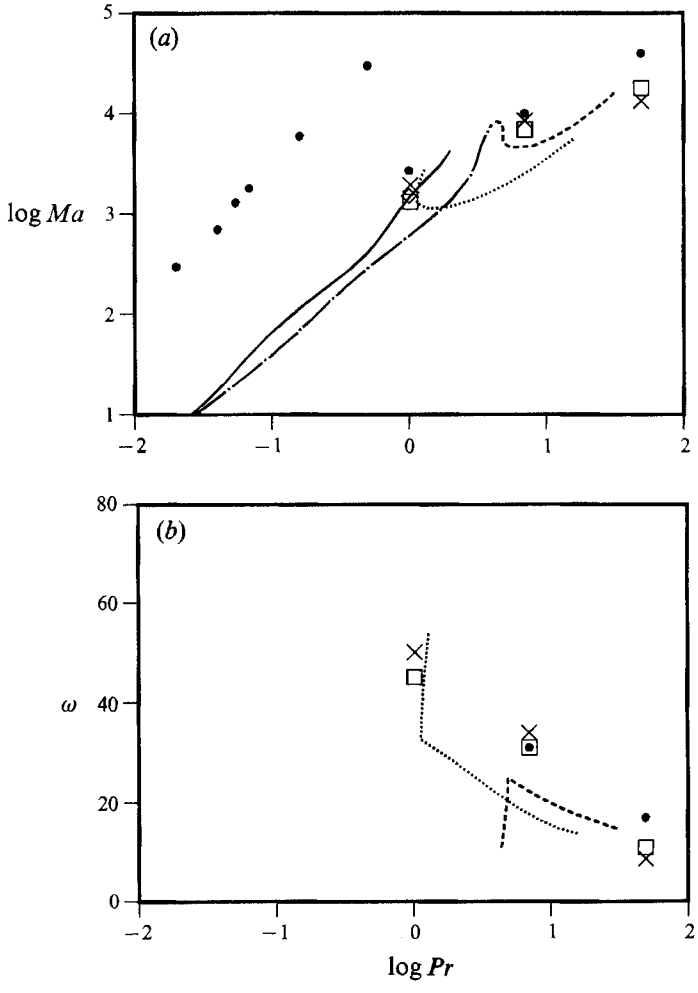

FIGURE 15. (*a*) Critical Marangoni number and (*b*) Hopf frequency versus Prandtl number for $\bar{m} = 1$, $Gr = 0$, and $\tilde{\Gamma} = 1$: ——, $B = 0$, $\omega_c = 0$; —·—·—, $B = 10$, $\omega_c = 0$; ····, $B = 0$, $\omega_c \neq 0$; – – –, $B = 10$; $\omega_c \neq 0$; other symbols as in figure 14.

Clearly, there are orders of magnitude between the first instability and the transition to time-dependent flow for small Pr. The strong turning of the large-Pr instability branches for $\bar{m} = 1$ and $\bar{m} = 2$ close to $Pr = 1$ explains the order of magnitude jump in the critical Marangoni number Ma_c^{osc} at which the transition to time-dependent flow (Rupp *et al.* 1989) occurs. Figure 15 underlines the importance of heat transfer at the free surface (here $\bar{m} = 1$), showing that a much better agreement between the numerical and the experimental stability boundary for $Pr = 7$ can be obtained, if heat loss is taken into account.

7. Summary and conclusions

The linear stability of two-dimensional thermocapillary flow in a non-isothermal liquid bridge has been investigated. Results have been obtained primarily for aspect ratio one. In all cases considered an increase of the surface tension Reynolds number

Re leads to a three-dimensional flow, which is steady for $Pr < 1$ and oscillatory for $Pr > 1$. The origin of the stationary instability is purely hydrodynamic, while the oscillatory modes can be identified as large-Pr hydrothermal waves. The critical azimuthal wavenumber for $\tilde{\Gamma} = 1$ was always found to be $\bar{m} = 1$. The stability boundary for the transition to steady three-dimensional flow with $\bar{m} = 1$ and for $Pr = 0.0078$ depends strongly on the aspect ratio and takes a relative minimum value of $Re_c = 350$ when $\tilde{\Gamma} = 1.1$. Heat loss through the free surface results in a decreased critical Reynolds number for the stationary instability (small Pr) and in an increased value of Re_c for the oscillatory instability (large Pr). The inclusion of weak buoyancy forces acts to stabilize both bifurcation branches if the liquid is heated from above and to destabilize if it is heated from below.

In the limit of small Pr the liquid bridge problem considered is similar to the problem of a driven cylindrical cavity, in which the flow is forced by imposing a constant axial velocity at $r = 1/\tilde{\Gamma}$ (Kuhlmann & Adabala 1993). From this analogy a similar stationary instability to that described in §5.2 can be expected for the mechanically forced system. The no-slip boundary conditions (especially in the axial direction at $r = 1/\tilde{\Gamma}$) for the disturbances in the latter system, however, may stabilize the axisymmetric flow to a considerable degree.

In view of the many difficulties in establishing well-defined conditions for the heat transfer, Reynolds number reduction due to contamination of the free surface, surface deformations, surface waves, and possibly non-Boussinesq effects, a quantitative agreement between theory and experiment cannot be expected at present. It has been shown, however, that the larger-Pr instability in finite-size liquid bridges is due to the hydrothermal wave instability as discussed by Smith (1983). The stationary low-Pr instability, which has not yet been studied experimentally, remains a subject for future investigations, as does extended high-accuracy calculations in the large Prandtl number limit.

The authors gratefully acknowledge the constructive comments of the referees.

REFERENCES

BARTEN, W., LÜCKE, M. & KAMPS, M. 1990 Conservation and breaking of mirror symmetry in a numerical simulation of vortex flow. *J. Comput. Phys.* **91**, 468.

CARPENTER, B. M. & HOMSY, G. M. 1989 Combined buoyant–thermocapillary flow in a cavity. *J. Fluid Mech.* **207**, 121.

CARPENTER, B. M. & HOMSY, G. M. 1990 High Marangoni number convection in a square cavity: Part II. *Phys. Fluids* A**2**, 137.

CHANG, C. E. & WILCOX, W. R. 1976 Analysis of surface tension driven flow in floating zone melting. *Intl J. Heat Mass Transfer* **19**, 355.

CHUN, C.-H. 1980 Experiments on steady and oscillatory temperature distribution in a floating zone due to the Marangoni convection. *Acta Astronautica* **7**, 479.

CLARK, P. A. & WILCOX, W. R. 1980 Influence of gravity on thermocapillary convection in floating zone melting of Silicon. *J. Cryst. Growth* **50**, 461.

CRÖLL, A., MÜLLER-SEBERT, W., BENZ, K. W. & NITSCHE, R. 1991 Natural and thermocapillary convection in partially confined silicon melt zones. *Microgravity Sci. Tech.* **3**, 204.

FU, B.-I. & OSTRACH, S. 1985 Numerical solutions of thermocapillary flows in floating zones. In *Transport Phenomena in Materials Processing, Power Eng. Div.* vol. 10, *Heat Transfer Div.* vol. 29, p. 1. ASME.

GARY, J. & HELGASON, R. 1970 A matrix method for ordinary differential eigenvalue problems. *J. Comput. Phys.* **5**, 169.

GOUSSIS, D. A. & PEARLSTEIN, A. J. 1989 Removal of infinite eigenvalues in a generalized matrix eigenvalue problem. *J. Comput. Phys.* **84**, 242.

HARDIN, G. R., SANI, R. L., HENRY, D. & ROUX, B. 1990 Buoyancy-driven instability in a vertical cylinder: Binary fluids with Soret effect. Part 1: General theory and stationary stability results. *Intl J. Num. Meth. Fluids* **10**, 79.

JONES, C. A. 1985*a* Numerical methods for the transition to wavy Taylor vortices. *J. Comput. Phys.* **61**, 321.

JONES, C. A. 1985*b* The transition to wavy Taylor vortices. *J. Fluid Mech.* **157**, 135.

KAMOTANI, Y., OSTRACH, S. & VARGAS, M. 1984 Oscillatory thermocapillary convection in a simulated floating – zone configuration. *J. Cryst. Growth* **66**, 83.

KAZARINOFF, N. D. & WILKOWSKI, J. S. 1990 Bifurcations of numerically simulated thermocapillary flows in axially symmetric float zones. *Phys. Fluids* A**2**, 1797.

KUHLMANN, H. 1989 Small amplitude thermocapillary flow and surface deformations in a liquid bridge. *Phys. Fluids* A**1**, 672.

KUHLMANN, H. C. & ADABALA, R. R. 1993 Biorthogonal series method for Oseen type flows. *Intl J. Engng Sci.* (to appear).

NEITZEL, G. P., CHANG, K.-T., JANKOWSKI, D. F. & MITTELMANN, H. D. 1992 Linear stability of thermocapillary convection in a model of float-zone crystal growth. *AIAA*-92-0604.

NEITZEL, G. P., LAW, C. C., JANKOWSKI, D. F. & MITTELMANN, H. D. 1991 Energy stability of thermocapillary convection in a model of the float-zone crystal-growth process. II: Nonaxisymmetric disturbances. *Phys. Fluids* A**3**, 2841.

PEARSON, J. R. A. 1958 On convection cells induced by surface tension. *J. Fluid Mech.* **4**, 489.

PETERS, G. & WILKINSON, J. H. 1970 $Ax = \lambda Bx$ and the generalized eigenproblem. *SIAM J. Num. Anal.* **7**, 479.

PREISSER, F., SCHWABE, D. & SCHARMANN, A. 1983 Steady and oscillatory thermocapillary convection in liquid columns with free cylindrical surface. *J. Fluid Mech.* **126**, 545.

RUPP, R., MÜLLER, G. & NEUMANN, G. 1989 Three-dimensional time dependent modelling of the Marangoni convection in zone melting configurations for GaAs. *J. Cryst. Growth* **97**, 34.

RYBICKI, A. & FLORYAN, J. M. 1987 Thermocapillary effects in liquid bridges. I. Thermocapillary convection. *Phys. Fluids* **30**, 1956.

SEN, A. K. & DAVIS, S. H. 1982 Steady thermocapillary flows in two-dimensional slots. *J. Fluid Mech.* **121**, 163.

SHEN, Y. 1989 Energy stability of thermocapillary convection in a model of float-zone crystal growth. Ph.D. thesis, Arizona State University.

SHEN, Y., NEITZEL, G. P., JANKOWSKI, D. F. & MITTELMANN, H. D. 1990 Energy stability of thermocapillary convection in a model of the float-zone crystal-growth process. *J. Fluid Mech.* **217**, 639.

SMITH, M. K. 1986*a* Thermocapillary and centrifugal-buoyancy-driven motion in a rapidly rotating liquid cylinder. *J. Fluid Mech.* **166**, 245.

SMITH, M. K. 1986*b* Instability mechanisms in dynamic thermocapillary liquid layers. *Phys. Fluids* **29**, 3182.

SMITH, M. K. 1988 The nonlinear stability of dynamic thermocapillary liquid layers. *J. Fluid Mech.* **194**, 391.

SMITH, M. K. & DAVIS, S. H. 1983*a* Instabilities of dynamic thermocapillary liquid layers. Part 1. Convective instabilities. *J. Fluid Mech.* **132**, 119.

SMITH, M. K. & DAVIS, S. H. 1983*b* Instabilities of dynamic thermocapillary liquid layers. Part 2. Surface-wave instabilities. *J. Fluid Mech.* **132**, 145.

VELTEN, R., SCHWABE, D. & SCHARMANN, A. 1991 The periodic instability of thermocapillary convection in cylindrical liquid bridges. *Phys. Fluids* A**3**, 267.

XU, J.-J. & DAVIS, S. H. 1983 Liquid bridges with thermocapillarity. *Phys. Fluids* **26**, 2880.

XU, J.-J. & DAVIS, S. H. 1984 Convective thermocapillary instabilities in liquid bridges. *Phys. Fluids* **27**, 1102.

ZEBIB, A., HOMSY, G. M. & MEIBURG, E. 1985 High Marangoni number convection in a square cavity. *Phys. Fluids* **28**, 3467.